

1 **A single-cell transcriptomic atlas characterizes liver**
2 **non-parenchymal cells in healthy and diseased mice**

3

4 Zheng Wang^{1†}, Jingyang Qian^{1†}, Xiaoyan Lu^{1†}, Ping Zhang¹, Rongfang Guo¹, He Lou¹,
5 Shuying Zhang², Jihong Yang³, Xiaohui Fan^{1,2,4*}

6

7 ¹ Pharmaceutical Informatics Institute, College of Pharmaceutical Sciences, Zhejiang
8 University, Hangzhou, 310058, China.

9 ² State Key Laboratory of Modern Chinese Medicine, Tianjin University of Traditional
10 Chinese Medicine, Tianjin 301617, China.

11 ³ Department of Medicine, Columbia Center for Human Development, Columbia
12 University Irving Medical Center, New York, NY, 10032, USA.

13 ⁴ iMedicine Lab, Alibaba-Zhejiang University Joint Research Center of Future Digital
14 Healthcare, Hangzhou 310058, China.

15 †These authors have contributed equally to this work

16 *To whom correspondence should be addressed. Tel: +86-571-88208596; Fax: +86-
17 571-88208426; E-mail: fanxh@zju.edu.cn

18

19

20

21 **ABSTRACT**

22 The heterogeneity of liver non-parenchymal cells (NPCs) is essential for liver structure
23 and function. However, the current understanding of liver NPCs, especially in different
24 liver diseases, remains incompletely elucidated. Here, a single-cell transcriptome atlas
25 of 171,814 NPCs from healthy and 5 typical liver disease mouse models, including
26 alcoholic liver disease, nonalcoholic steatohepatitis (NASH), drug-induced liver injury,
27 cholestatic, and ischemia-reperfusion liver injury is constructed. The inter- and intra-
28 group heterogeneity of 12 types (and numerous subtypes) of NPCs involving
29 endothelial cells, hepatic stellate cells (HSCs), neutrophils, T cells, and mononuclear
30 phagocytes (MPs) are summarized. A protective subtype of neutrophils characterized
31 by *Chil3^{high}* is validated and found significantly increasing only in drug-induced and
32 cholestatic liver injury models. Transcriptional regulatory network analysis reveals
33 disease-specific transcriptional reprogramming. Metabolic activity analysis indicates
34 that fibrosis is accompanied by increases in glycolysis and retinol metabolism in
35 activated HSCs and MPs. Moreover, we found that cell-cell interactions between
36 cholangiocytes and immune cells contribute more to cholestatic liver fibrosis compared
37 with NASH, while HSCs are more important for NASH fibrosis. Our atlas, together
38 with an interactive website provides a systematic view of highly heterogeneous NPCs
39 and a valuable resource to better understand pathological mechanisms underlying liver
40 diseases.

41

42

43

44 INTRODUCTION

45 The liver is a complex ecosystem, composed of diverse types of cells, that plays vital
46 metabolic and immunological functions (1). Despite considerable improvements over
47 past decades, liver diseases remain a major public health challenge worldwide.
48 Alcoholic liver disease (ALD), nonalcoholic fatty liver disease (NAFLD), drug-
49 induced liver injury (DILI), cholestatic liver injury, and liver ischemia-reperfusion (IR)
50 injury caused by surgery together account for over 70% of the incidence of liver
51 diseases, seriously affecting the quality of human life (2). A major obstacle for
52 development of precision therapies for liver disease is our lack of systematical
53 understanding of the ecosystem, especially in different liver diseases.

54 Almost all types of liver disease are accompanied by an inflammatory response (3).
55 Liver non-parenchymal cells (NPCs), including mononuclear phagocytes (MPs),
56 endothelial cells (ECs), hepatic stellate cells (HSCs), cholangiocytes, and other
57 infiltrated inflammatory cells (e.g. neutrophils), are essential for the liver structure,
58 function, and response to inflammatory liver injury (4). MPs are composed of Kupffer
59 cells (KCs), monocyte-derived macrophages (MoMFs), and dendritic cells (DCs) (4).
60 KCs, resident macrophages, play a key role in liver inflammation. After activation, KCs
61 adopt M1-like pro-inflammatory macrophage or M2-like anti-inflammatory
62 macrophage functions in response to liver injury (3). Recruited MoMFs, which are
63 divided according to pro-inflammatory (M1) and wound-healing (M2) phenotypes, also
64 play a role in acute and chronic liver inflammation (3). Although KCs and MoMFs have
65 similarities, they can be distinguished by numerous markers (3). Neutrophils also play
66 essential roles in acute and chronic inflammation (5). These inflammatory cells also
67 have interaction with HSCs through specific ligand-receptor pairs (6). Inflammatory
68 activities of these inflammatory cells induce HSCs activation (from the resting
69 phenotype to a myofibroblast-like phenotype), which is the major cause of liver fibrosis
70 (7). Activated HSCs themselves promote further liver inflammation and fibrosis, which
71 is characterized by increased cell proliferation, the secretion of pro-inflammatory
72 cytokines, and an enhancement in the synthesis of extracellular matrix (ECM) (3). Thus,
73 liver NPCs show considerable cellular diversity, and their crosstalk plays an important
74 role in liver disease. Although it is well known that NPCs regulate various aspects of
75 the occurrence and progression of liver disease, the cellular heterogeneity and dynamic
76 regulation of NPCs needs to be studied at a single-cell resolution to better understand
77 the pathological mechanism of liver disease.

78 Single-cell RNA sequencing (scRNA-seq) provides a new perspective for
79 understanding the physiological and pathological processes of multicellular organism
80 (8). By defining the transcriptomic landscape of cells, scRNA-seq can reveal the role
81 of intercellular communication in health and disease at an unprecedented resolution (4).
82 Recently, a diverse range of studies involving scRNA-seq have revealed the
83 heterogeneity of healthy human liver cells (9), explored the distinctive functional
84 composition of infiltrating T cells in hepatocellular carcinoma (10), delineated the
85 transcriptomic landscape and intercellular crosstalk in human intrahepatic
86 cholangiocarcinoma (11), and revealed the heterogeneity of individual cell types and
87 their crosstalk during fibrogenesis in both fibrotic mice and nonalcoholic steatohepatitis

88 (NASH) patients (12). However, a complete single-cell landscape of liver NPCs
89 including health and multiple liver diseases has not been disclosed, and differences in
90 NPCs among these different typical mouse models of liver disease need to be clarified.

91 In this study, we used the 10x Genomics scRNA-seq platform to profile single cells
92 from healthy mouse and diseased murine livers. The diseased livers were obtained from
93 various mouse models of liver disease, including ALD, 45% high fat-
94 methionine/choline deficient (HF-MCD) diet-induced NASH, bile duct ligation (BDL)-
95 induced cholestatic liver injury, acetaminophen (APAP)-induced DILI, and liver IR
96 injury. Using these data, we aimed to provide a comprehensive transcriptomic overview
97 of NPCs from healthy and diseased murine livers, investigate the heterogeneity of liver
98 NPCs, clarify the differences between the assessed disease models, and developed an
99 interactive website (<http://tcm.zju.edu.cn/mlna>) to provide universal access to this data
100 source. Together, our findings provide a valuable resource to better understand the
101 pathological mechanisms underlying liver diseases and for clinical therapeutics.

102

103 **MATERIALS AND METHODS**

104 **Animals**

105 Eight- to twelve-week-old male C57BL/6J mice were purchased from Charles River
106 Laboratories (Beijing, China). Mice were maintained in specific pathogen-free facilities
107 (12-hour light/dark cycle) with access to food and water *ad libitum*. All animal
108 experiments were performed following procedures approved by the Animal Care and
109 Use Committee of Zhejiang University.

110

111 **Animal models of liver disease**

112 *Model Construction of ALD.* The mouse model of ALD by chronic-plus-binge ethanol
113 feeding was described previously (13). Briefly, mice initially received the control
114 Lieber-DeCarli diet (Bio-Serv, Cat#F1259SP) for 5 days to accommodate to a liquid
115 diet, which was followed by acclimation to the ethanol Lieber-DeCarli ethanol liquid
116 diet (Bio-Serv, Cat#F1258SP) of 5% (v/v) ethanol for 2 weeks. On the final day of
117 feeding, an additional gavage of ethanol (5 g kg⁻¹, Aladdin Biochemical, Cat#E111993)
118 was administered to mice in the early morning. After 9 hours of gavage, mice were
119 anesthetized for subsequent experiments.

120

121 *Model Construction of NASH.* The long-term feeding of choline deficiency combined
122 with high-fat diet was developed to recapitulate key features of human NASH (14). To
123 construct the NASH model, mice were feed on a MCD diet containing 45% kcal fat
124 (Research Diets, Cat#A06071301B) for 8 weeks as previously described (15), which
125 preferable maintained the increase of mice body weight. The normal chow diet fed mice
126 were treated as control.

127

128 *Model Construction of Liver IR Injury.* An established mouse model of 70% warm
129 hepatic IR injury was used (16). Briefly, the hepatic artery and portal vein were isolated
130 and clipped with a microvascular clamp, occluding blood supply to the left and middle
131 liver lobes. After 45 minutes of ischemia, the clamp was removed to initiate the

132 reperfusion phase. Mice were sacrificed at 24 hours after reperfusion

133

134 *Model Construction of APAP-induced Acute Liver Injury.* Acute liver injury was
135 induced by APAP overdose in mice (17). Before APAP treatment, mice were fasted for
136 approximately 16 hours. Then the animals were intraperitoneally injected once with
137 APAP (300 mg kg⁻¹, TCI, Cat#H0190) dissolved in 25% propylene glycol (Sinopharm
138 Chemical Reagent, Cat#30157018) and saline solution. At 24 hours after APAP
139 administration, livers were obtained to be processed for further experiments.

140

141 *Model Construction of BDL-induced Cholestatic Liver Injury.* Cholestasis in the
142 experimental model was induced by BDL surgery in mice as previously performed (18).
143 Under general anesthesia, mice were placed supine for midline laparotomy to expose
144 the common bile duct. Then bile duct ligation was performed in two adjacent positions
145 approximately 1 cm from the porta hepatis with 6-0 silk sutures. The duct was then
146 severed by incision between the two sites of ligation. On the tenth day after bile duct
147 ligation, the liver was harvested to isolate NPCs.

148

149 **Isolation of Liver NPCs and Preparation of Single-cell Suspensions**

150 Liver NPCs were isolated from mice according to a two-step collagenase method
151 reported previously (6). In detail, murine livers were perfused *in situ* via the inferior
152 vana cava with calcium-free Hank's Balanced Salt Solution (HBSS, Gibco,
153 Cat#14170112) containing EDTA (0.2 mg mL⁻¹, Sigma, Cat#E6758), followed by the
154 buffer II containing pronase (0.4 mg mL⁻¹, Sigma, Cat#P5147-1G) and 0.2%
155 collagenase type II (Worthington, Cat#LS004176) at a perfusion rate of 8 mL/minute.
156 Then livers were surgically removed and cut into small pieces. Tissues were transferred
157 in HBSS containing 0.2% collagenase type II, pronase (0.4 mg mL⁻¹) and DNase I (0.1
158 mg mL⁻¹, Roche, Cat#10104159001), and then incubated for digestion at 37 °C in a
159 water bath for 20 minutes. DMEM (Mediatech, Cat#10-013-CV) containing 10%
160 serum (FBS, Gibco, Cat#10099-141C) was added at the end of the incubation.
161 Sequentially, hepatocytes removal was achieved by centrifugation for 3 minutes at 50
162 g. Then cell suspension was filtered using a 40 µm nylon cell strainer (Falcon,
163 Cat#352340). Erythrocytes were lysed by treatment with 3-5 mL ACK lysing buffer
164 (Gibco, Cat#A1049201) for 5 minutes, after which PBS (Beyotime Biotec,
165 Cat#C0221A) was added to terminate the lysis. The resulting suspension was subjected
166 to Dead Cell Removal Kit (Miltenyi Biotec, Cat#130090101) to remove dead cells
167 according to the manufacturer's recommendations. The obtained cell pellet was washed
168 twice and resuspended in PBS. Cell viability was assessed by Trypan Blue (Gibco,
169 Cat#15250-061).

170

171 **10x Genomics scRNA-seq**

172 Liver NPCs single cell suspensions were loaded onto the 10x Genomics Chromium
173 chip (10x Genomics; Pleasanton, CA, USA) to generate droplets. Then the obtained
174 Gel Beads-in-emulsion (GEMs) were transferred into a PCR tube strip, followed by
175 reverse transcription using ProFlex PCR System (Thermo Fisher, MA, USA). The

176 resulting cDNA was purified and amplified for 12 cycles before cleanup with
177 SPRIselect beads (Beckman, Cat#B23318). Based on the cDNA concentration
178 determined by Qubit (Thermo Fisher, MA, USA), libraries were prepared using the
179 Chromium Single Cell 3' Library & Gel Bead Kit v3 (10x Genomics; Pleasanton, CA,
180 USA) according to the manufacturer's instructions. All the libraries were sequenced on
181 the Illumina Novaseq platform by Novogene (Beijing, China).

182

183 **Histological Assessment of Liver Sections**

184 Retrieved liver tissues from sacrificed mice were placed immediately in 10% formalin
185 solution. After embedded in paraffin, tissue sections were cut at 5 μ m thickness
186 followed by deparaffinization in xylene and rehydration in 100%, 95%, 90%, 80%, 75%
187 alcohol successively. Then the sections were incubated with 3% H₂O₂ to inactive
188 endogenous peroxidases for 10 minutes in the dark at room temperature. Nonspecific
189 binding blocking was performed with 5% BSA for 1 hour. Next, slides were stained
190 with hematoxylin and eosin (H&E) for morphological evaluation, and were stained with
191 Sirius Red for fibrosis assessment. For immunochemical analysis, slides were
192 incubated with primary antibodies against LYVE1 (1:2000, Abcam, Cat#218535) at 4 °C
193 overnight in the dark. After three times of PBS washing for 5 minutes, the
194 corresponding *horseradish peroxidase* (HRP)-conjugated Goat anti-Rabbit IgG
195 secondary antibody (Origene, Cat#PV-6002) was sequentially used for incubation at
196 room temperature for 30 minutes. Nuclei were counterstained with hematoxylin. The
197 expression pattern of LYVE1 in liver slides was acquired by Olympus BX63
198 microscope (Olympus, Shinjuku, Japan) at 200x magnification.

199

200 **Immunofluorescence Staining**

201 Liver sections were cut into 5 μ m slides from formalin-fixed and paraffin-embedded
202 tissues dissected from C57BL/6J mice. The slides were incubated with the primary
203 antibody against S100A9 (1:500, Abcam, Cat#ab242945) at 4 °C overnight. After slide
204 washing with PBS-T (PBS + 0.05% Tween20), the fluorophore-conjugated secondary
205 antibodies were used for incubation at room temperature for 1.5 hours. For double
206 immunostaining, liver sections were firstly stained with CD31 (1:500, Abcam,
207 Cat#ab182981) or S100A9 (1:500, Abcam, Cat#ab242945) followed by the appropriate
208 secondary antibody. Then LYVE1 (1:1000, Abcam, Cat#ab218535) or YM1 (1:500,
209 Abcam, Cat#192029) antibody was applied onto sections following the identical
210 procedure. Tissue slides were mounted with Antifade Mounting Medium with DAPI
211 (Origene, Cat#ZU9557) for nuclei staining. Fluorescence images were captured with
212 an Olympus BX63 microscope. The fluorophore-conjugated secondary antibodies
213 include Goat anti-Rabbit IgG H&L-Alexa Fluor 488 (1:500, Abcam, Cat#ab150077)
214 and Goat anti-Rabbit IgG H&L-Alexa Fluor 555 (1:500, Abcam, Cat#ab150078)

215

216 **Data Processing**

217 The gene expression matrix for each scRNA-seq sample was generated by CellRanger
218 pipeline (10x Genomics) and raw data were processed further in R (version 3.6.1).
219 Quality filtering steps were performed using the Seurat package (version 3.1.2) (19):

- 220 1. Genes expressed by less than 5 cells were excluded from further analysis.
- 221 2. Cells with fewer than 200 genes expressed, and > 20% of total expression from
- 222 mitochondrial genes were filtered out.

223 Through the above steps, 197,194 cells were used for next analysis. For filtered gene
224 expression matrices, gene counts for each cell were normalized by dividing by the total
225 counts for that cell and multiplying by the scale.factor (10,000) with the NormalizeData
226 function of the Seurat package. In order to remove the batch effect, the top 2,000 highly
227 variable genes were used for canonical correlation analysis (CCA) implemented in
228 Seurat.

229

230 **Clustering and Cell Typing**

231 After aligning the top 20 dimensions according to CCA, principal component analysis
232 (PCA) was used to reduce dimension using the RunPCA function, and unsupervised
233 clustering was applied using the FindNeighbors function and the FindClusters function
234 with default parameters. Cells were later visualized using the RunTSNE function with
235 the t-distributed stochastic neighbor embedding (t-SNE) algorithm. We then calculated
236 the top marker genes for each cluster using the Wilcoxon rank-sum test, by the
237 FindAllMarkers function (logfc.threshold = 1.5, min.pct = 0.25). The identity for each
238 cluster was annotated based on the SingleR package (version 1.0.5)(20) and the prior
239 knowledge of biology. The cells expressing high levels of classic hepatocyte marker
240 genes (*Alb*, *Apoa2*, *Apoc3* and *Mup3*) were filtered out. A total of 171,814 cells
241 remained finally. For sub-clustering of each major liver cell type, a higher “resolution”
242 parameter of FindClusters function was applied. We also used the FindAllMarkers
243 function (logfc.threshold = 0.25, min.pct = 0.25, test.use = “wilcox”) to perform
244 differential expression analysis for each subcluster.

245

246 **Pseudo-cell Analysis**

247 As described and confirmed before (21), we performed pseudo-cell analysis to increase
248 the gene expression correlation from high-throughput scRNA-seq data. Briefly, we built
249 a new gene expression matrix for each cell type by constructing pseudo-cells, which
250 were the averages of 20 cells randomly chosen.

251

252 **Transcription Factor-target Gene Network Analysis**

253 The regulatory network analysis was performed on pseudo-cell gene expression
254 matrices using the SCENIC package (version 1.1.2-01, corresponds to GENIE3 1.8.0,
255 RcisTarget 1.6.0 and AuCell 1.8.0)(22) with default parameters. Two gene-motif
256 rankings databases of mouse (10 kb around the TSS and 500 bp upstream of TSS) were
257 selected for RcisTarget. To determine the number of “on/off” regulons in each cell type
258 on different models, we set the criteria as follow:

- 259 1. we used “mean (AUC scores)” for each regulon as threshold to binarize the
260 regulon activity scores and created the binary regulon activity matrix, where 1
261 for “on” and 0 for “off”.
- 262 2. In each cell type, if the binary activity of the regulon was “on” in more than half
263 of cells, we considered this regulon was “on” in the cell type.

264 The transcription factor-target gene network was visualized with Cytoscape (version
265 3.7.2).

266

267 **Deconvolution of Liver Microarray/Bulk-seq Data**

268 To accessed the MPs composition in different liver diseases, we applied deconvolution
269 analysis on publicly available microarray/bulk-seq data from annotated liver biopsy
270 specimens taken across the AH (GSE28619), the APAP induced ALF (GSE120652),
271 the BA (GSE159720), the IR injury (GSE151648) and the NAFLD (GSE48452). In
272 particularly, all control samples from 5 datasets were collected together as control group.
273 We only chose the IRI⁺ samples as IR group and the nonalcoholic steatohepatitis
274 samples as NASH group. MPs from our scRNA-seq data were clustered into KCs,
275 MoMFs and DCs, and signature gene expression profiles of these 3 cell types were used
276 to deconvolve the MPs composition of different liver disease samples using
277 CIBERSORTx (23). The composition of MoMFs of different liver disease samples was
278 later associated with the histological features provided by original research paper.

279

280 **Pathway Enrichment Analysis**

281 Pathway enrichment analysis was performed using the Gene Ontology (GO) biological
282 process and pathway terms in Metascape (version 3.5)(24) (<http://metascape.org>) with
283 default parameters, as well as Ingenuity Pathway Analysis (IPA). The results were
284 visualized with the ggplot2 package (version 3.3.0).

285

286 **CCI Analysis**

287 Pseudo-cell gene expression matrices were input to predict CCI based on the pseudo-
288 cell gene expression matrices using CellPhoneDB (version 1.1.0) (25). The ligands or
289 receptors which expressed in at least 10% of cells were considered only. For all ligand-
290 receptor pairs, only those with average expression > 0.1 as well as *p*-value < 0.1 were
291 selected for subsequent prediction. To explore immune activation of non-immune cells
292 in different groups, for each type of non-immune cells (endothelial cell, HSC and
293 cholangiocyte), we selected the shared interactions between it and each immune cell
294 type of six major cell types (B cell, MPs, neutrophil, NK, pDC and T cell). We also
295 analyzed the expression levels of immune genes in non-immune cells in different
296 groups. A totally 2484 immune genes in 17 major categories were obtained from
297 ImmPort database (<https://www.immport.org>). Based on the result of Sirius Red
298 staining, we chose the ligand/receptor genes in two fibrosis-related categories
299 “TGFβ_Family_Member” and “TGFβ_Family_Member_Receptor” to perform the
300 CCI analysis between non-immune cells and immune cells in BDL and HF-MCD
301 groups.

302

303 **Metabolic Analysis**

304 We used the method published before to characterize the metabolic heterogeneity in
305 different cell types and groups (26). Totally 1,664 metabolic genes and 85 pathways
306 were obtained from the KEGG database (<http://www.kegg.jp>), and the metabolic
307 pathways were further grouped into specific categories based on KEGG classifications.

308 The pathway activities were calculated following the protocol using the pseudo-cell
309 gene expression matrices.

310

311 **Pseudotime Analysis**

312 Pseudotime analysis was performed on neutrophil (Neu1, Neu2, and Neu3) and kupffer
313 subtypes (MP1, MP2, and MP3) using the monocle R package (version 2.14.0) (27).
314 Genes expressed in less than 10 cells were removed. After reducing the dimensionality
315 of the data using the DDRTree dimensionality reduction algorithm with the
316 reduceDimension function, cell ordering was performed by the orderCells function to
317 build the trajectory. We then calculated the genes differentially expressed along the
318 pseudotime with the differentialGeneTest function and selected those with significant
319 differences (q -value < 0.05). For Kupffer cell, we also verified the trajectory and its
320 directionality using the velocity (version 0.17) (28). We generated annotated spliced
321 and unspliced reads matrices from 10x bam files and selected the aimed cells based on
322 the cell typing result to estimate cell velocities. We set the neighborhood size as 500
323 cells and all other parameters were default.

324

325 **Statistical Analyses**

326 Marker genes for each cell cluster were calculated by the FindAllMarkers function in
327 Seurat R package using the Wilcoxon rank-sum test. Genes with q -value < 0.05 were
328 considered statistically enriched in a cluster. For metabolic pathways analysis, we
329 evaluated the activities of metabolic pathways in a specific cell type by using the
330 random permutation test. Only the pathways with p -value < 0.05 were considered
331 statistically changed in different cell types or groups. For CCI analysis, the interaction
332 with p -value < 0.1 , mean expression > 0.1 was indicated statistically significant. For
333 calculating the genes differentially expressed along the trajectory in pseudotime
334 analysis, the genes with significant differences were selected based on q -value < 0.05 .
335 For plasma biochemical parameters, the significance of differences between control
336 group and model group was determined by two-tailed Student's t -test using Graph-Pad
337 Prism v5.0, the p -value < 0.05 was considered statistically significant.

338

339 **RESULTS**

340 **An overview of the single-cell atlas of murine liver NPCs**

341 To obtain an overall landscape and compare the cell heterogeneity of liver NPCs in
342 various disease models at a single-cell level, we successfully established 5 classic
343 models of liver disease and performed scRNA-seq on livers from these disease groups
344 and a control group using the 10x Genomics platform (Figure 1A; Supplementary
345 Figure S1A and Table S1). We subsequently developed an interactive website “Murine
346 liver NPCs Atlas” to provide universal access to this data source. Through the browsing
347 function, we can know the expression of clinically important genes related to diseases
348 in different cell types.

349 All liver cells were isolated from mice according to a previously described method,
350 which has a higher collection rate for NPCs (6). After quality control analysis, we
351 obtained 197,194 single-cell transcriptomes in total, which include 25,380 hepatocytes

352 and 171,814 NPCs from 18 mice (3 mice per group) in the control and 5 liver disease
353 groups (Figure 1B and C; Supplementary Figure S1B and C). Clustering analysis of
354 NPCs was subsequently performed using gene expression profiles. The t-distributed
355 stochastic neighbor embedding (t-SNE) plot was used to visualize 12 major clusters of
356 NPCs based on the expression of marker genes (Figure 1B and E; Supplementary
357 Figure S1D). The distribution and proportions of the 12 major cell types in each group
358 provide an insight into the disease groups. For example, an obvious opposite trend was
359 observed in the numbers of ECs in the ALD and HF-MCD groups, and neutrophils were
360 notably increased in the APAP and BDL groups compared with the other groups (Figure
361 1D). Likewise, the numbers of MPs in the BDL group showed a difference in
362 distribution compared with those in the control group, indicating that some subclusters
363 of MPs may be increased in the BDL group (Figure 1B and C). Clustering analysis of
364 12 NPCs clusters confirmed several unique transcriptomic characteristics (Figure 1E).
365 For instance, PECAM1 (CD31) and LYVE1 are already well-known ECs markers, and
366 S100A9 is often used as a neutrophil marker (6,29). Consistent with our analysis results,
367 an immunofluorescence staining experiment with PECAM1 and LYVE1 and
368 immunohistochemical staining of LYVE1 confirmed the opposite trend in ALD and
369 HF-MCD groups (Figure 1F and G; Supplementary Figure S1E). Similarly, a dramatic
370 increase in the neutrophil number in the APAP and BDL groups was verified by S100A9
371 staining (Figure 1H and Supplementary Figure S1F). These results provide an overview
372 of the differences in NPCs in the murine livers among different classic liver diseases.

373

374 **Reconstruction and heterogeneity of transcriptional regulatory networks in** 375 **disease groups**

376 To understand the regulatory networks of transcriptional factors (TFs) in cell types and
377 to determine the differences between groups, we predicted the relevant TFs and binarize
378 the activity scores of TFs. We then counted the number of TFs with activity “on” and
379 that of TFs with activity “off” in each cell type. In most cell types, the number of TFs
380 with activity “on” was increased in disease groups (compared with that in the control
381 group), although there were obvious differences among the disease groups (Figure 2A).
382 The heat map of the activity of TFs revealed that, in each cell type (e.g. ECs or
383 neutrophils), the up-regulated TFs demonstrated an inter-group specificity (Figure 2B
384 and C; Supplementary Figure S2).

385 We found that most TFs for ECs up-regulated in the ALD group were down-regulated
386 in the HF-MCD group observably, including *Egr1*, *Snai1*, and *Bcl6b*, which are related
387 to angiogenesis, vascular development, and cell growth (Figure 2B and D). However,
388 up-regulated TFs in the HF-MCD group, such as *Foxp1*, are associated with cell death
389 and negative regulation of vascular development according to gene ontology (GO)
390 analysis (Figure 2B and D). These results may partially explain the observed opposite
391 trend of ECs numbers between the ALD and HF-MCD groups presented in Figure 1D.
392 In the IR group, up-regulated TFs (*Irf2*, *Irf8*, *Stat1*, and *Stat2*) of ECs are related to the
393 defense response and innate immune response based on the GO analysis (Figure 2B).
394 This is consistent with the characteristics of IR injury. Although inflammation-related
395 neutrophils were dramatically increased in both APAP and BDL groups compared to

396 the control group, neutrophil TFs were differentially regulated (Figure 1D and Figure
397 2C). TFs (*Fos*, *Atf3*, and *Nfe2l2*) related to acute inflammation and oxidative stress were
398 up-regulated in the APAP group and down-regulated in the BDL group (Figure 2C and
399 E). In contrast, TFs (*Irf1*, *Stat1*, and *Stat2*) related to innate immunity, adaptive
400 immunity, and defense response were up-regulated in the BDL group and down-
401 regulated in the APAP group (Figure 2C and E). In the IR group, the TFs up-regulated
402 in neutrophils were similar to those up-regulated in ECs (Figure 2B, C, and E). Together,
403 these data demonstrate that specific diseases reprogram transcriptional regulatory
404 networks and that there is a heterogeneity among disease groups.

405

406 **The inter- and intra-group heterogeneity of NPCs**

407 Here, we performed detailed subtype annotation and functional analysis mainly on ECs,
408 HSCs, neutrophils, T cells, MPs, and cholangiocytes. ECs were divided into six
409 subtypes at a higher t-SNE resolution based on their unique transcriptomic signatures:
410 four subtypes (Endo1-Endo4) of LSECs and two subtypes (Endo5 and Endo6) of
411 pericentral (Endo-pc) and periportal (Endo-pp) ECs (Figure 3A-C). LSECs are
412 characterized by two known LSECs markers (*Gpr182* and *Fcgr2b*) (30). Although
413 transcriptomes of LSECs are similar in general, some genes are highly expressed in a
414 subtype-specific manner (Figure 3C). In addition to two conventional LSEC subtypes
415 (Endo1 and Endo2), GO analysis demonstrated that Endo3 and Endo4 are related to the
416 inflammatory response and adaptive immune response, respectively. Furthermore,
417 *Clqa* (a marker of Endo3) was found to stimulate ECs proliferation and promote new
418 vessel formation (31). The group proportions in ECs subtypes were similar to those in
419 ECs (Figure 1D and Figure 3C). Liver fibrosis-associated HSCs were divided into four
420 subtypes, containing quiescent HSCs (HSC1) and activated HSCs (HSC2, HSC3, and
421 HSC4) based on specific markers (Figure 3D-F). Interestingly, GO analysis showed
422 distinguishable functions of HSC2 and HSC3, HSC2 are related to wounding response
423 and ECM organization, while HSC3 are related to inflammatory response and
424 cholesterol metabolic process. All three neutrophil subtypes (Neu1, Neu2, and Neu3)
425 with distinct transcriptomic signatures were dramatically increased in APAP and BDL
426 groups (Figure 3G-I). Evidence is accumulating that neutrophils have different
427 phenotypes and characteristics even in a highly mature state (32). According to the IPA,
428 Neu1 promotes an inflammatory response and cell migration, while Neu2 and Neu3
429 downregulate inflammation and cell movement (Figure 3J). *Mmp8* (a marker of Neu2)
430 is highly expressed in mature neutrophils and to play a beneficial role in chronic and
431 cholestasis liver injury by alleviating fibrosis (33). Likewise, *Chil3* (*Ym1*, a marker of
432 Neu3) is a known marker of M2 macrophages, and *Ly6g*⁺ neutrophils play an anti-
433 inflammatory role in allergic mice (34). Furthermore, our immunofluorescence staining
434 experiment has verified the abundant presence of protective Neu3 subtype in BDL and
435 APAP groups (Figure S4). The subtypes of infiltrated neutrophils in the tissue
436 demonstrates the development of neutrophil heterogeneity and reprogramming of
437 neutrophils from a pro-inflammatory phenotype to an anti-inflammatory phenotype
438 (35). To determine whether neutrophils have polarization for homeostasis maintenance
439 in response to inflammation, we analyzed the pseudotime polarization trajectory of

440 these three neutrophil subtypes. We found that the infiltrated neutrophils demonstrate a
441 polarization trajectory from Neu1 to Neu3 (Figure 3K). Hence, our results demonstrate
442 the existence of protective neutrophil subtypes and neutrophil polarization.

443 Similarly, 30,120 T cells were divided into seven subtypes, including natural killer T
444 (NKT) cells (T1), CD4⁺ T cells (T2, T3, and T4), CD8⁺ T cells (T5 and T6), and specific
445 Ramp1⁺ T cells (T7), with distinct transcriptomic signatures (Figure 4A-C). In
446 particular, the number of subtypes T3 (CD4⁺ Foxp3⁺ regulatory T cells) and T6 (effector
447 memory CD8⁺ T cells) was notably elevated in the HF-MCD group, which consistent
448 with previous studies that activated CD4⁺ and CD8⁺ T cells is essential for the
449 progression of NASH and liver fibrosis (Figure 4C) (14,36). T4 and T5 are naive CD4⁺
450 and CD8⁺ T cells with high expression of *Ccr7* and *Sell* (10). Finally, a specific subtype
451 of Ramp⁺ T cells was also identified, which plays a role in angiogenesis according to
452 GO analysis. The role of T cells in angiogenesis and vasculogenesis has previously been
453 noted under pathological and physiological conditions (37). MPs, the largest cell type
454 of NPCs, were divided into eight subtypes based on their unique transcriptomic markers,
455 including KCs (MP1-MP4), MoMFs (MP5 and MP6), and conventional dendritic cells
456 (cDCs) (MP7 and MP8) (Figure 4D-F) (4,6,38). MP3 is a type of periodic KC
457 characterized by high expression of *Stmn1* (Figure 4F) (38). Trem2 and Chil3 are well-
458 known markers of pro- and anti- inflammatory macrophages, respectively (6,38).
459 Ingenuity Pathway Analysis (IPA) analysis was used to confirm that Trem2⁺ MoMFs
460 (MP5) up-regulated the inflammatory response pathways and Chil3⁺ MoMFs (MP6)
461 down-regulated those inflammatory response pathways (Figure 4G). Cholangiocytes
462 are an important type of intrahepatic NPCs that participate in bile production and
463 homeostasis (39). Cholangiocytes were divided into four subtypes (Cho1-Cho4) using
464 distinctive transcriptomic markers (Figure 4H-J). Besides, cell types including NK cells
465 (Figure S3A-C), dividing cells (Figure S3D-F), B cells (Figure S3G-I), and
466 plasmacytoid dendritic cells (pDCs) (Figure S3J-L) were divided into different cell
467 subtypes according to their individual transcriptomic signatures. Altogether, above
468 results demonstrate the heterogeneity of NPCs in the liver.

469 As recruited macrophages, MoMFs play important regulatory roles in a variety of
470 liver injury (3). To determine whether MoMFs expand in various human liver diseases
471 as we found in mouse models, we analyzed liver RNA sequencing data of patients with
472 NASH, alcoholic hepatitis (AH), IR injury after liver transplantation, APAP-induced
473 acute liver failure (ALF), and biliary atresia (BA). We applied differential gene
474 expression signatures of KCs, MoMFs, and DCs to the deconvolution algorithm to
475 evaluate the composition of MPs in human liver (Supplementary Figure S5A and B).
476 Results showed abundant expansion of MoMFs in patients with NASH, IR injury,
477 APAP-induced ALF, and BA, which is consistent with our findings (Supplementary
478 Figure S5A-C). With the increase of MoMFs, the histological NAFLD activity score
479 (NAS), fibrosis score, and inflammation score deteriorated (Supplementary Figure
480 S5D). It indicated that the expansion of MoMFs positively correlated with the progress
481 of NASH and the degree of fibrosis.

482 Furthermore, one of the advantages of scRNA-seq technology is to understand the
483 characterization of gene expression in different cell types/subtypes. In order to

484 determine the expression characteristics of disease-related clinically significant genes
485 in different cell types/subtypes, we analyzed the gene expression of a series of blood
486 markers and drug targets for NASH diagnosis and therapy in each cell type. Cytokeratin
487 18 (CK18) is a blood marker of apoptosis and fibrosis for diagnosis of NASH (40). We
488 found that *Krt18*, which encodes CK18, is specifically high expressed in cholangiocytes
489 and obviously increased in subtype Cho3 in HF-MCD group (Supplementary Figure
490 S5E and F), suggesting that NASH is accompanied by significant injury and apoptosis
491 of cholangiocytes, especially subtype Cho3, and cholangiocytes may associate with the
492 mechanism of NASH. Galectin 3 (Gal-3) is one of the promising targets involved in
493 fibrosis for NASH treatment in clinical trials (40). We found that the gene expression
494 of *Lgals3* (encoding Gal-3) is increased in cell types of MPs and HSCs in the HF-MCD
495 group (Supplementary Figure S5G). Moreover, the expression of *Lgals3* is elevated in
496 subtypes of KCs, MoMFs, and HSC2 in the HF-MCD group (Supplementary Figure
497 S5H), implying that it not only reminds the importance of these three cell subtypes to
498 liver fibrosis, but also provides more precise guiding significance for the development
499 of drugs with Gal3 as the drug target. Altogether, these indicated the clinical value of
500 our scRNA-seq data.

501

502 **Metabolic reprogramming of NPCs across disease groups**

503 Considering that the liver plays an important role in regulating energy metabolism in
504 the whole body, the metabolic reprogramming of NPCs in liver disease states is worth
505 investigating. The hepatic immune response includes the enhanced glucose metabolism
506 of immunocompetent cells (41). HSCs show a particularly high sensitivity, and they
507 play an important role in immune metabolism by maintaining liver function and
508 responding to injury (42). Next, we investigated the features of metabolic pathway
509 reprogramming of NPCs in different disease groups by quantifying metabolic pathway
510 activity based on a previously described pathway activity score (26). The pathways
511 investigated included those for carbohydrate metabolism, energy metabolism, lipid
512 metabolism, etc. Almost all metabolic pathways in cholangiocytes were dramatically
513 activated in the BDL group (Figure 5A). This is consistent with the pathological
514 mechanism of cholestatic liver injury induced by ligation of the bile duct, in which the
515 siltation and reflux of bile aggravates cholangiocyte stimulation and subsequent
516 damage. In addition, numerous metabolic pathways in HSCs and MPs, including the
517 carbohydrate, energy, lipid, etc. metabolic pathways, were activated (compared with
518 control) in the BDL, IR, and HF-MCD groups (Figure 5A and B). This suggests that
519 the metabolic activation of HSCs and MPs is required to exert an appropriate immune
520 effect. Interestingly, NK cells were only activated in the IR group, suggesting that NK
521 cells have specific metabolic activity in IR liver injury (Figure 5B). Next, through
522 analysis of the metabolism in subtypes of MPs, HSCs, and NK cells in each disease
523 group, we found that the metabolic activity of subtypes KCs, HSC2, and NK3 was the
524 strongest in BDL, IR, and HF-MCD groups (Supplementary Figure S6A-C).

525 Energy metabolism is essential in activated HSCs to support a multitude of functions,
526 including proliferation, secretion of ECM and cytokines, and migration to the injury
527 regions. In addition, carbohydrate and lipid metabolism are required for the activation

528 of HSCs, because transdifferentiation into the myofibroblast phenotype requires
529 upregulation of glycolysis and depletion of retinol-containing cytoplasmic lipid
530 droplets to meet energy demands (42). To understand further, we analyzed gene
531 expression of glycolytic and retinol metabolism pathway in each cell type in different
532 groups (Supplementary Figure S7A and B). We observed that the gene expression of
533 inhibition of glycolysis (*Fbp1*) was down-regulated, while genes expression of
534 promotion of glycolysis and retinol metabolism (*Eno2*, *Eno3* and *Rdh5*, *Aox1*) were
535 elevated in HSCs in HF-MCD and BDL groups (Figure 5C) (43-45). These results
536 confirm the abovementioned metabolic up-regulation and demonstrate the inter-group
537 heterogeneity of HSCs activation. Besides, the expression of glycolysis-related genes
538 was up-regulated in MPs (to varying degrees) in BDL, IR, and HF-MCD groups (Figure
539 5D). The expression of these genes in different cell subtypes can be further explored on
540 our website. These findings reveal the heterogeneity of the metabolic reprogramming
541 of NPCs in different liver diseases, especially confirm the importance of metabolic
542 activation of HSCs and MPs in liver disease.

543

544 **Inter-group heterogeneity in communication between non-immune cells** 545 **and immune cells**

546 Cell-cell interaction (CCI) is a basic feature of multicellular organisms, playing an
547 essential role in numerous biological processes (46). The construction of a CCI network
548 based on ligand-receptor interaction is a common strategy for analyzing scRNA-seq
549 data (46). Non-immune NPCs, including ECs, cholangiocytes, and HSCs, also play a
550 role in immune activation by communicating with immune cells and thus influencing
551 pathological progression (47). To evaluate the global participation of non-immune cells
552 in the immune response, we investigated the expression of immune-related genes in
553 ECs, cholangiocytes, and HSCs and constructed a model of the CCI network between
554 non-immune and immune cells in different disease groups (Figure 6). We found that
555 expression levels of immune-related genes, especially those encoding
556 chemokines/cytokines and their receptors, were up-regulated in ECs, cholangiocytes,
557 and HSCs and that the different disease states show differential expression (Figure 6A).

558 After comparison of CCI networks between non-immune and immune cells in
559 different groups, we observed a notable increase of CCIs in most disease groups
560 compared to the control group and the number of interactions between HSCs, ECs,
561 cholangiocytes and different intrahepatic immune cells showed an inter-group
562 heterogeneity (Figure 6B and C; Supplementary Figure S8A and B). Moreover, we
563 identified unique ligand-receptor pairs of the CCI in each model group compared with
564 control and found differences in ligand-receptor pairs between model groups (Figure
565 6D and Supplementary Figure S8C). Functions of unique ligand-receptor pairs in HSCs
566 are mostly related to immunity, inflammatory response, cell proliferation, apoptosis,
567 and transdifferentiation (Figure 6D). Surprisingly, expression level of the ligand-
568 receptor pair CCL5-GPR75 was specifically enhanced, the interaction between them
569 was only observed between immune cells (especially NK and T cells) and HSCs in IR
570 and HF-MCD groups (Figure 6D). These findings indicate the inter-group
571 heterogeneity in the immune activation of non-immune cells.

572

573 **Inter-group cell heterogeneity in transcriptional dynamics**

574 KCs are resident macrophages found throughout the mammalian liver and play
575 essential roles in liver disease (47). To investigate the inter-group heterogeneity of KCs
576 polarization process and of KCs transcriptional dynamics, we analyzed polarization
577 trajectories of three KC subtypes using monocle2 and RNA velocity methods for
578 pseudotime ordering. We observed a polarization trajectory from periodic KC subtype
579 MP3 to MP1 to MP2 in all groups (except the APAP group, which had rarely population
580 of KCs) (Figure 7A and B). A similar polarization trajectory was inferred using the
581 RNA velocity method, with KCs polarization in the HF-MCD group being the most
582 obvious (Figure 7B). Next, we investigated genes with dramatically perturbed
583 expression along this trajectory in each group and identified 501 genes common to all
584 groups (Figure 7C and D). Interestingly, we found that the expression of apoptosis-
585 related genes *Bax* and *Bcl2a1b* was up-regulated and of anti-proliferation factors *Btg1*
586 and *Btg2* was markedly reduced along the trajectory in the control group, while
587 completely opposite trend was observed in HF-MCD, BDL, and APAP groups (Figure
588 7E). Furthermore, as the trajectory changes, expression levels of inflammation-related
589 genes (*Ccl5*, *Ccl2*, *Cxcl2*, and *Trem2*) and fibrosis-related genes (*Tgfb1* and *Tgfb2*)
590 were markedly increased in HF-MCD, BDL, and APAP groups (Figure 7E). Together,
591 these results indicate that the polarization of KCs in the healthy liver is highly correlated
592 with periodic proliferation and apoptosis, while in disease, periodic KCs are polarized
593 into functional KCs to play important roles in progression of liver disease.

594

595 **DISCUSSION**

596 Liver diseases, including DILI, cholestatic liver injury, liver IR injury, ALD, and NASH,
597 are associated with extremely high morbidity and mortality worldwide, causing a huge
598 social burden (2). APAP-induced DILI is the most common and clinically relevant
599 model of intrinsic DILI (48). BDL is the most widely used classic experimental model
600 of cholestasis (49). Liver IR injury has been considered as a potential mechanism
601 responsible for organ dysfunction and injury after liver surgery such as liver
602 transplantation (50). The ALD model was constructed based on a method published in
603 *Nature Protocols*, which describes the generation of a simple and effective ALD model
604 with no mortality rate, no liver fibrosis, marked elevation of alanine aminotransferase
605 and steatosis (13). The pathology of NASH can be induced by the MCD diet rather than
606 a high-fat diet (HFD) in C57BL/6J mice (14). MCD diet is a valuable tool for
607 investigating the inflammatory effects in NASH due to its availability and
608 simplification (51). Inadequate intake of methionine/choline can lead to defective
609 lipoprotein secretion and oxidative stress caused by impaired β -oxidation in the liver,
610 and further induce hepatic steatosis, inflammation and fibrosis (14,51). However, mice
611 fed the MCD diet will not develop any metabolic diseases associated with obesity or
612 insulin resistance, and even loss weight (52). Thus, the MCD diet cannot fully
613 recapitulate the characteristics of NASH patients. Nonetheless, since at least 90% of
614 Americans do not meet the recommended choline intake, and choline deficiency in
615 NASH patients can lead to more severe fibrosis, we applied a 45% HF-MCD diet to

616 investigate characteristics of NASH (53,54).

617 This study provided new insights into liver physiology and pathology through single-
618 cell transcriptomic technologies. Here, we obtained a comprehensive single-cell
619 transcriptomic landscape of NPCs from livers of healthy and diseased mice, and
620 constructed a website to provide simple access to all our data. Through analysis of
621 distribution and proportions of ECs cluster in each group, we observed that the number
622 of ECs was markedly reduced only in the HF-MCD group, even though both ALD and
623 HF-MCD involve steatosis (Figure 1D, F, and G; Supplementary Figure S1A and E).
624 Thus, ECs injury is a characteristic of the HF-MCD group, which is in agreement with
625 a previous study (6), and ECs injury may related to the degree of liver steatosis and
626 fibrosis. Furthermore, although ECs were greatly reduced in the HF-MCD group, the
627 CCI between ECs and immune cells was notably increased (Figure 6B and
628 Supplementary Figure S8A), indicating that ECs injury is associated with an
629 enhancement in CCI. ECs injury in the HF-MCD group also showed regional
630 heterogeneity, which represented that the damage to LSECs was greater than the
631 damage to Endo-pc and Endo-pp, and the LSEC population was decreased compared
632 with the Endo-pc and Endo-pp populations (Figure 3C).

633 Neutrophils are considered as main mediators of the inflammatory response during
634 tissue injury. Even though a dramatic infiltration of neutrophils was observed in both
635 APAP and BDL groups, the number of MoMFs was only markedly increased in the
636 BDL group (extremely low in the APAP group), implying that the main cell type
637 involved in the inflammatory response is different in APAP- and BDL-induced liver
638 injury (Figure 3I and Figure 4F). Recent evidence suggests that infiltrated neutrophils
639 can polarize into a protective phenotype, which exerts an anti-inflammatory effect and
640 restores homeostasis (55). Here, we verified the existence of protective neutrophil
641 subtype and analyzed the polarization trajectory of neutrophils from Neu1 to Neu3
642 subtype (Figure 3K and Supplementary Figure S4). The number of activated CD4⁺ and
643 CD8⁺ T cells was greatly increased in the HF-MCD group (Figure 4C), which is
644 consistent with clinical results suggesting that CD8⁺ T cells are increased in the livers
645 of NASH patients (56). Moreover, NKT cells play a role in the fibrotic progression of
646 NASH, and activation of CD8⁺ T cells and NKT cells can lead to NASH via crosstalk
647 with hepatocytes (14), indicating that T cells play an important role in progressive
648 NASH. In order to further explore the clinical application value of our data, we
649 compared our data with publicly available bulk RNA-seq data from human liver
650 diseases. Due to the limitations of analytical method, we only obtained the consistent
651 result of the increase in the proportion of MoMFs at a lower resolution (Supplementary
652 Figure S5A-C). We can further analyze to complement the present database, when
653 human single-cell data of these liver diseases are available later.

654 The CCI analysis demonstrated that immune activation of non-immune cells had
655 heterogeneity between different disease groups. In comparison with the control,
656 differences in specific ligand-receptor pairs involved in immune and non-immune cell
657 interactions were observed in each model group. For instance, the interactions between
658 CXCL10 and CXCR3, and CXCL10 and DPP4 (from HSCs to immune cells) were
659 specific for the BDL group, while the interaction between CXCL10 and DPP4 (from

660 immune cells to HSCs) was specific to the HF-MCD group (Figure 6D). *Tgfb2*
661 (transforming growth factor beta 2) is known as a positive regulator of liver fibrosis
662 and is a participant in biliary-induced liver disease based on previous data obtained
663 from a BDL mouse model (57). In agreement with these observations, our results
664 demonstrate that only cholangiocytes in the BDL group showed a high expression of
665 *Tgfb2* and its receptor *TgfbR2*. However, in the HF-MCD group, ECs and HSCs (rather
666 than cholangiocytes) showed a high expression of *Tgfb2* and *TgfbR2* (Figure 6A).
667 Considering that liver fibrosis was obvious in both the BDL and HF-MCD groups, we
668 investigated differences in the gene expression of *Tgfb* family members between these
669 groups (Supplementary Figure S8D and E). *Tgfb* family genes were highly expressed
670 in cholangiocytes in the BDL group, and in HSCs and ECs in the HF-MCD group.
671 Moreover, while fibrosis-related CCIs between cholangiocytes and immune cells in the
672 BDL group were stronger (compared with the HF-MCD group), CCIs between HSCs
673 and immune cells were more obvious in the HF-MCD group (Figure S8F). These results
674 indicate that cholangiocytes are mainly responsible for cholestatic liver fibrosis (58),
675 while HSCs mainly contribute to the fibrosis in NASH. Although the total number of
676 cells collected in the APAP group was the lowest, the reasons for the greatly reduced
677 CCIs in the APAP group need to be explored further.

678 In conclusion, we first have provided here, a comprehensive single-cell
679 transcriptomic landscape of murine liver NPCs in health and 5 liver disease models
680 (representing more than 70% incidence of liver disease). Although more disease models
681 and the single-cell spatiotemporal heterogeneity of intrahepatic cells, including
682 hepatocytes, should be considered in the future study, this study has prominently
683 increased our understanding of the physiological and pathological mechanisms
684 underlying liver function and dysfunction, and should contribute to the clinical
685 diagnosis and therapeutics of liver diseases.

686

687 **DATA AVAILABILITY**

688 All raw single-cell RNA sequencing data in this paper have been deposited into the
689 Gene Expression Omnibus (GEO) database (GEO: GSE166178). The raw or processed
690 data can be downloaded on the GEO database or our website
691 (<http://tcm.zju.edu.cn/mlna>). Custom code for analysis will be available by request.

692

693 **SUPPLEMENTARY DATA**

694 Supplementary Data are available at NAR Online.

695

696 **ACKNOWLEDGEMENTS**

697 Z.W. designed, performed, and analyzed all experiments; J.Q. processed scRNA-seq
698 data and performed computational analysis; P.Z., R.G., H.L., and S.Z. participated in
699 the experiment; Z.W., J.Q., P.Z., and J.Y. wrote the manuscript; X.L. and X.F. supported
700 and supervised the experiment and revised the manuscript; X.F. conceptualized the
701 study. All the authors reviewed the manuscript.

702

703 **FUNDING**

704 This work was supported by the National Natural Science Foundation of China
705 (81973701 to X.F., 81903767 to Z.W.), the Natural Science Foundation of Zhejiang
706 Province (LZ20H290002 to X.F.), and the National Youth Top-notch Talent Support
707 Program (W02070098 to X.F.).

708 *Conflict of interest statement.* None declared.

709

710 REFERENCES

- 711 1. Marrone, G., Shah, V.H. and Gracia-Sancho, J. (2016) Sinusoidal
712 communication in liver fibrosis and regeneration. *Journal of hepatology*, **65**,
713 608-617.
- 714 2. Wang, F.S., Fan, J.G., Zhang, Z., Gao, B. and Wang, H.Y. (2014) The global
715 burden of liver disease: the major impact of China. *Hepatology*, **60**, 2099-2108.
- 716 3. Koyama, Y. and Brenner, D.A. (2017) Liver inflammation and fibrosis. *The*
717 *Journal of clinical investigation*, **127**, 55-64.
- 718 4. Ramachandran, P., Matchett, K.P., Dobie, R., Wilson-Kanamori, J.R. and
719 Henderson, N.C. (2020) Single-cell technologies in hepatology: new insights
720 into liver biology and disease pathogenesis. *Nature reviews. Gastroenterology*
721 *& hepatology*, **17**, 457-472.
- 722 5. Castanheira, F.V.S. and Kubes, P. (2019) Neutrophils and NETs in modulating
723 acute and chronic inflammation. *Blood*, **133**, 2178-2185.
- 724 6. Xiong, X., Kuang, H., Ansari, S., Liu, T., Gong, J., Wang, S., Zhao, X.Y., Ji, Y.,
725 Li, C., Guo, L. *et al.* (2019) Landscape of Intercellular Crosstalk in Healthy and
726 NASH Liver Revealed by Single-Cell Secretome Gene Analysis. *Molecular cell*,
727 **75**, 644-660 e645.
- 728 7. Ceni, E., Mello, T., Polvani, S., Vasseur-Cognet, M., Tarocchi, M., Tempesti, S.,
729 Cavalieri, D., Beltrame, L., Marroncini, G., Pinzani, M. *et al.* (2017) The orphan
730 nuclear receptor COUP-TFII coordinates hypoxia-independent proangiogenic
731 responses in hepatic stellate cells. *Journal of hepatology*, **66**, 754-764.
- 732 8. Xiong, X., Kuang, H., Liu, T. and Lin, J.D. (2020) A Single-Cell Perspective of
733 the Mammalian Liver in Health and Disease. *Hepatology*, **71**, 1467-1473.
- 734 9. Aizarani, N., Saviano, A., Sagar, Mailly, L., Durand, S., Herman, J.S., Pessaux,
735 P., Baumert, T.F. and Grun, D. (2019) A human liver cell atlas reveals
736 heterogeneity and epithelial progenitors. *Nature*, **572**, 199-204.
- 737 10. Zheng, C., Zheng, L., Yoo, J.K., Guo, H., Zhang, Y., Guo, X., Kang, B., Hu, R.,
738 Huang, J.Y., Zhang, Q. *et al.* (2017) Landscape of Infiltrating T Cells in Liver
739 Cancer Revealed by Single-Cell Sequencing. *Cell*, **169**, 1342-1356 e1316.
- 740 11. Zhang, M., Yang, H., Wan, L., Wang, Z., Wang, H., Ge, C., Liu, Y., Hao, Y.,
741 Zhang, D., Shi, G. *et al.* (2020) Single-cell transcriptomic architecture and
742 intercellular crosstalk of human intrahepatic cholangiocarcinoma. *Journal of*
743 *hepatology*, **73**, 1118-1130.
- 744 12. Terkelsen, M.K., Bendixen, S.M., Hansen, D., Scott, E.A.H., Moeller, A.F.,
745 Nielsen, R., Mandrup, S., Schlosser, A., Andersen, T.L., Sorensen, G.L. *et al.*
746 (2020) Transcriptional Dynamics of Hepatic Sinusoid-Associated Cells After
747 Liver Injury. *Hepatology*.

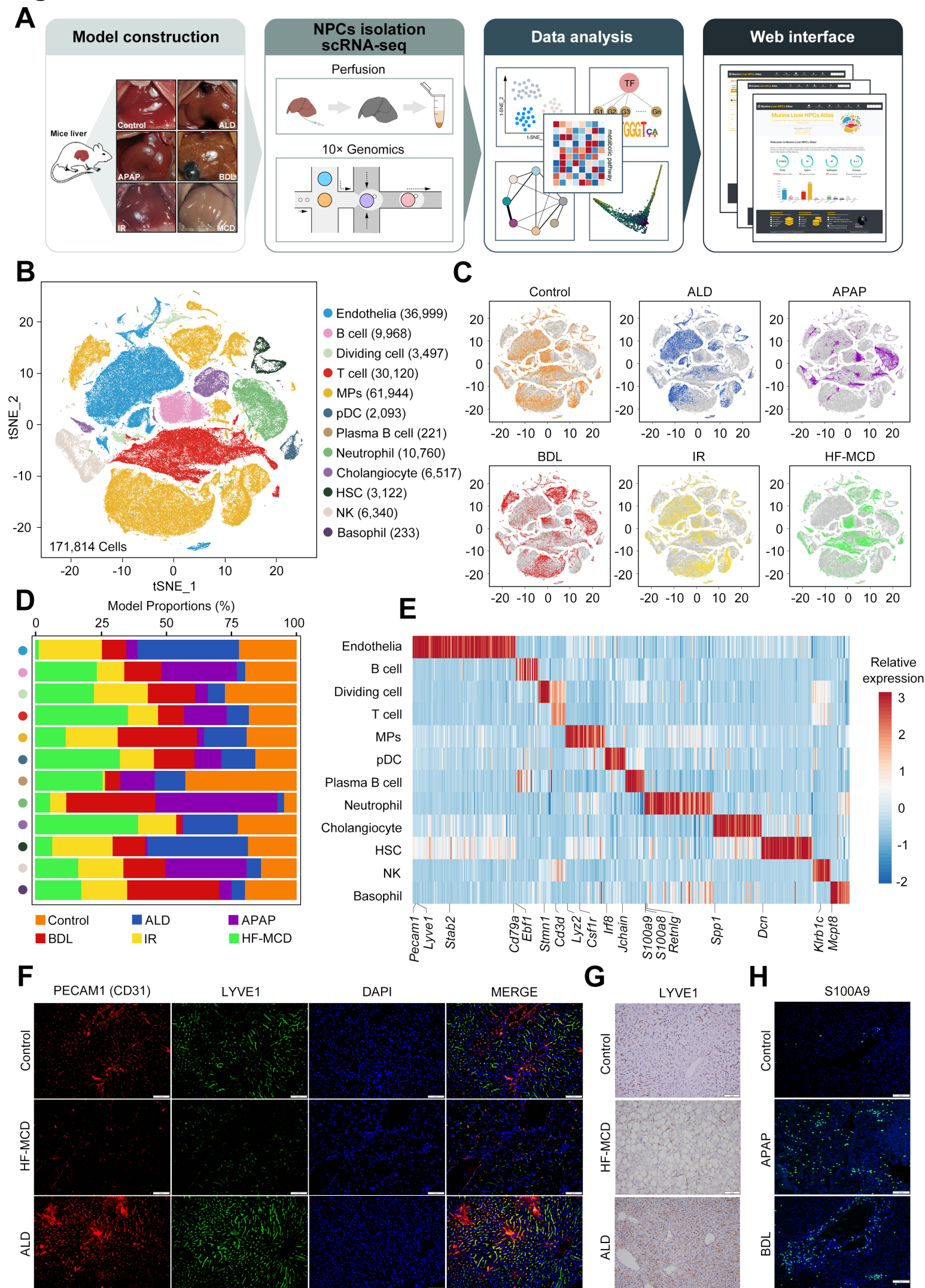
- 748 13. Bertola, A., Mathews, S., Ki, S.H., Wang, H. and Gao, B. (2013) Mouse model
749 of chronic and binge ethanol feeding (the NIAAA model). *Nature protocols*, **8**,
750 627-637.
- 751 14. Wolf, M.J., Adili, A., Piotrowitz, K., Abdullah, Z., Boege, Y., Stemmer, K.,
752 Ringelhan, M., Simonavicius, N., Egger, M., Wohlleber, D. *et al.* (2014)
753 Metabolic activation of intrahepatic CD8+ T cells and NKT cells causes
754 nonalcoholic steatohepatitis and liver cancer via cross-talk with hepatocytes.
755 *Cancer cell*, **26**, 549-564.
- 756 15. Xu, B., Jiang, M., Chu, Y., Wang, W., Chen, D., Li, X., Zhang, Z., Zhang, D.,
757 Fan, D., Nie, Y. *et al.* (2018) Gasdermin D plays a key role as a pyroptosis
758 executor of non-alcoholic steatohepatitis in humans and mice. *Journal of*
759 *hepatology*, **68**, 773-782.
- 760 16. Wang, Z., Zhang, P., Wang, Q., Sheng, X., Zhang, J., Lu, X. and Fan, X. (2020)
761 Protective effects of Ginkgo Biloba Dropping Pills against liver
762 ischemia/reperfusion injury in mice. *Chinese medicine*, **15**, 122.
- 763 17. Mossanen, J.C. and Tacke, F. (2015) Acetaminophen-induced acute liver injury
764 in mice. *Laboratory animals*, **49**, 30-36.
- 765 18. Ding, B.S., Cao, Z., Lis, R., Nolan, D.J., Guo, P., Simons, M., Penfold, M.E.,
766 Shido, K., Rabbany, S.Y. and Rafii, S. (2014) Divergent angiocrine signals from
767 vascular niche balance liver regeneration and fibrosis. *Nature*, **505**, 97-102.
- 768 19. Butler, A., Hoffman, P., Smibert, P., Papalexi, E. and Satija, R. (2018)
769 Integrating single-cell transcriptomic data across different conditions,
770 technologies, and species. *Nature biotechnology*, **36**, 411-420.
- 771 20. Aran, D., Looney, A.P., Liu, L., Wu, E., Fong, V., Hsu, A., Chak, S., Naikawadi,
772 R.P., Wolters, P.J., Abate, A.R. *et al.* (2019) Reference-based analysis of lung
773 single-cell sequencing reveals a transitional profibrotic macrophage. *Nature*
774 *immunology*, **20**, 163-172.
- 775 21. Han, X., Zhou, Z., Fei, L., Sun, H., Wang, R., Chen, Y., Chen, H., Wang, J.,
776 Tang, H., Ge, W. *et al.* (2020) Construction of a human cell landscape at single-
777 cell level. *Nature*, **581**, 303-309.
- 778 22. Aibar, S., Gonzalez-Blas, C.B., Moerman, T., Huynh-Thu, V.A., Imrichova, H.,
779 Hulselmans, G., Rambow, F., Marine, J.C., Geurts, P., Aerts, J. *et al.* (2017)
780 SCENIC: single-cell regulatory network inference and clustering. *Nature*
781 *methods*, **14**, 1083-1086.
- 782 23. Newman, A.M., Steen, C.B., Liu, C.L., Gentles, A.J., Chaudhuri, A.A., Scherer,
783 F., Khodadoust, M.S., Esfahani, M.S., Luca, B.A., Steiner, D. *et al.* (2019)
784 Determining cell type abundance and expression from bulk tissues with digital
785 cytometry. *Nature biotechnology*, **37**, 773-782.
- 786 24. Zhou, Y., Zhou, B., Pache, L., Chang, M., Khodabakhshi, A.H., Tanaseichuk,
787 O., Benner, C. and Chanda, S.K. (2019) Metascape provides a biologist-oriented
788 resource for the analysis of systems-level datasets. *Nature communications*, **10**,
789 1523.
- 790 25. Vento-Tormo, R., Efremova, M., Botting, R.A., Turco, M.Y., Vento-Tormo, M.,
791 Meyer, K.B., Park, J.E., Stephenson, E., Polanski, K., Goncalves, A. *et al.* (2018)

- 792 Single-cell reconstruction of the early maternal-fetal interface in humans.
793 *Nature*, **563**, 347-353.
- 794 26. Xiao, Z., Dai, Z. and Locasale, J.W. (2019) Metabolic landscape of the tumor
795 microenvironment at single cell resolution. *Nature communications*, **10**, 3763.
- 796 27. Qiu, X., Mao, Q., Tang, Y., Wang, L., Chawla, R., Pliner, H.A. and Trapnell, C.
797 (2017) Reversed graph embedding resolves complex single-cell trajectories.
798 *Nature methods*, **14**, 979-982.
- 799 28. La Manno, G., Soldatov, R., Zeisel, A., Braun, E., Hochgerner, H., Petukhov, V.,
800 Lidschreiber, K., Kastrioti, M.E., Lonnerberg, P., Furlan, A. *et al.* (2018) RNA
801 velocity of single cells. *Nature*, **560**, 494-498.
- 802 29. Han, X., Wang, R., Zhou, Y., Fei, L., Sun, H., Lai, S., Saadatpour, A., Zhou, Z.,
803 Chen, H., Ye, F. *et al.* (2018) Mapping the Mouse Cell Atlas by Microwell-Seq.
804 *Cell*, **172**, 1091-1107 e1017.
- 805 30. Poisson, J., Lemoine, S., Boulanger, C., Durand, F., Moreau, R., Valla, D. and
806 Rautou, P.E. (2017) Liver sinusoidal endothelial cells: Physiology and role in
807 liver diseases. *Journal of hepatology*, **66**, 212-227.
- 808 31. Bossi, F., Tripodo, C., Rizzi, L., Bulla, R., Agostinis, C., Guarnotta, C., Munaut,
809 C., Baldassarre, G., Papa, G., Zorzet, S. *et al.* (2014) C1q as a unique player in
810 angiogenesis with therapeutic implication in wound healing. *Proceedings of the
811 National Academy of Sciences of the United States of America*, **111**, 4209-4214.
- 812 32. Xie, X., Shi, Q., Wu, P., Zhang, X., Kambara, H., Su, J., Yu, H., Park, S.Y., Guo,
813 R., Ren, Q. *et al.* (2020) Single-cell transcriptome profiling reveals neutrophil
814 heterogeneity in homeostasis and infection. *Nature immunology*, **21**, 1119-1133.
- 815 33. Harty, M.W., Huddleston, H.M., Papa, E.F., Puthawala, T., Tracy, A.P., Ramm,
816 G.A., Gehring, S., Gregory, S.H. and Tracy, T.F., Jr. (2005) Repair after
817 cholestatic liver injury correlates with neutrophil infiltration and matrix
818 metalloproteinase 8 activity. *Surgery*, **138**, 313-320.
- 819 34. Nowroozilarki, N., Oz, H.H., Schroth, C., Hector, A., Nurnberg, B., Hartl, D.
820 and Kolahian, S. (2018) Anti-inflammatory role of CD11b(+)Ly6G(+)
821 neutrophilic cells in allergic airway inflammation in mice. *Immunology letters*,
822 **204**, 67-74.
- 823 35. Garcia-Culebras, A., Duran-Laforet, V., Pena-Martinez, C., Moraga, A.,
824 Ballesteros, I., Cuartero, M.I., de la Parra, J., Palma-Tortosa, S., Hidalgo, A.,
825 Corbi, A.L. *et al.* (2019) Role of TLR4 (Toll-Like Receptor 4) in N1/N2
826 Neutrophil Programming After Stroke. *Stroke*, **50**, 2922-2932.
- 827 36. Her, Z., Tan, J.H.L., Lim, Y.S., Tan, S.Y., Chan, X.Y., Tan, W.W.S., Liu, M.,
828 Yong, K.S.M., Lai, F., Ceccarello, E. *et al.* (2020) CD4(+) T Cells Mediate the
829 Development of Liver Fibrosis in High Fat Diet-Induced NAFLD in Humanized
830 Mice. *Frontiers in immunology*, **11**, 580968.
- 831 37. Simons, K.H., Aref, Z., Peters, H.A.B., Welten, S.P., Nossent, A.Y., Jukema,
832 J.W., Hamming, J.F., Arens, R., de Vries, M.R. and Quax, P.H.A. (2018) The
833 role of CD27-CD70-mediated T cell co-stimulation in vasculogenesis,
834 arteriogenesis and angiogenesis. *International journal of cardiology*, **260**, 184-
835 190.

- 836 38. Ramachandran, P., Dobie, R., Wilson-Kanamori, J.R., Dora, E.F., Henderson,
837 B.E.P., Luu, N.T., Portman, J.R., Matchett, K.P., Brice, M., Marwick, J.A. *et al.*
838 (2019) Resolving the fibrotic niche of human liver cirrhosis at single-cell level.
839 *Nature*, **575**, 512-518.
- 840 39. Banales, J.M., Huebert, R.C., Karlsen, T., Strazzabosco, M., LaRusso, N.F. and
841 Gores, G.J. (2019) Cholangiocyte pathobiology. *Nature reviews.*
842 *Gastroenterology & hepatology*, **16**, 269-281.
- 843 40. Romero, F.A., Jones, C.T., Xu, Y., Fenaux, M. and Halcomb, R.L. (2020) The
844 Race to Bash NASH: Emerging Targets and Drug Development in a Complex
845 Liver Disease. *Journal of medicinal chemistry*, **63**, 5031-5073.
- 846 41. Meszaros, K., Bojta, J., Bautista, A.P., Lang, C.H. and Spitzer, J.J. (1991)
847 Glucose utilization by Kupffer cells, endothelial cells, and granulocytes in
848 endotoxemic rat liver. *The American journal of physiology*, **260**, G7-12.
- 849 42. Trivedi, P., Wang, S. and Friedman, S.L. (2020) The Power of Plasticity-
850 Metabolic Regulation of Hepatic Stellate Cells. *Cell metabolism*.
- 851 43. Cong, J., Wang, X., Zheng, X., Wang, D., Fu, B., Sun, R., Tian, Z. and Wei, H.
852 (2018) Dysfunction of Natural Killer Cells by FBP1-Induced Inhibition of
853 Glycolysis during Lung Cancer Progression. *Cell metabolism*, **28**, 243-255 e245.
- 854 44. Zhong, G., Seaman, C.J., Paragas, E.M., Xi, H., Herpoldt, K.L., King, N., Jones,
855 J.P. and Isoherranen, N. (2020) Aldehyde Oxidase Contributes to all-trans-
856 Retinoic Acid Biosynthesis in Human Liver. *Drug metabolism and disposition:*
857 *the biological fate of chemicals*.
- 858 45. Liu, C.C., Wang, H., Wang, W.D., Wang, L., Liu, W.J., Wang, J.H., Geng, Q.R.
859 and Lu, Y. (2018) ENO2 Promotes Cell Proliferation, Glycolysis, and
860 Glucocorticoid-Resistance in Acute Lymphoblastic Leukemia. *Cellular*
861 *physiology and biochemistry : international journal of experimental cellular*
862 *physiology, biochemistry, and pharmacology*, **46**, 1525-1535.
- 863 46. Shao, X., Lu, X., Liao, J., Chen, H. and Fan, X. (2020) New avenues for
864 systematically inferring cell-cell communication: through single-cell
865 transcriptomics data. *Protein & cell*, **11**, 866-880.
- 866 47. Heymann, F. and Tacke, F. (2016) Immunology in the liver--from homeostasis
867 to disease. *Nature reviews. Gastroenterology & hepatology*, **13**, 88-110.
- 868 48. McGill, M.R. and Jaeschke, H. (2019) Animal models of drug-induced liver
869 injury. *Biochimica et biophysica acta. Molecular basis of disease*, **1865**, 1031-
870 1039.
- 871 49. Mariotti, V., Strazzabosco, M., Fabris, L. and Calvisi, D.F. (2018) Animal
872 models of biliary injury and altered bile acid metabolism. *Biochimica et*
873 *biophysica acta. Molecular basis of disease*, **1864**, 1254-1261.
- 874 50. Nastos, C., Kalimeris, K., Papoutsidakis, N., Tasoulis, M.K., Lykoudis, P.M.,
875 Theodoraki, K., Nastou, D., Smyrniotis, V. and Arkadopoulos, N. (2014) Global
876 consequences of liver ischemia/reperfusion injury. *Oxidative medicine and*
877 *cellular longevity*, **2014**, 906965.
- 878 51. Reid, D.T. and Eksteen, B. (2015) Murine models provide insight to the
879 development of non-alcoholic fatty liver disease. *Nutrition research reviews*, **28**,

- 880 133-142.
- 881 52. Hebbard, L. and George, J. (2011) Animal models of nonalcoholic fatty liver
882 disease. *Nature reviews. Gastroenterology & hepatology*, **8**, 35-44.
- 883 53. Zeisel, S.H., Klatt, K.C. and Caudill, M.A. (2018) Choline. *Advances in*
884 *nutrition*, **9**, 58-60.
- 885 54. Guerrero, A.L., Colvin, R.M., Schwartz, A.K., Molleston, J.P., Murray, K.F.,
886 Diehl, A., Mohan, P., Schwimmer, J.B., Lavine, J.E., Torbenson, M.S. *et al.*
887 (2012) Choline intake in a large cohort of patients with nonalcoholic fatty liver
888 disease. *The American journal of clinical nutrition*, **95**, 892-900.
- 889 55. Hou, Y., Yang, D., Xiang, R., Wang, H., Wang, X., Zhang, H., Wang, P., Zhang,
890 Z., Che, X., Liu, Y. *et al.* (2019) N2 neutrophils may participate in spontaneous
891 recovery after transient cerebral ischemia by inhibiting ischemic neuron injury
892 in rats. *International immunopharmacology*, **77**, 105970.
- 893 56. Bhattacharjee, J., Kirby, M., Softic, S., Miles, L., Salazar-Gonzalez, R.M.,
894 Shivakumar, P. and Kohli, R. (2017) Hepatic Natural Killer T-cell and CD8+ T-
895 cell Signatures in Mice with Nonalcoholic Steatohepatitis. *Hepatology*
896 *communications*, **1**, 299-310.
- 897 57. Dropmann, A., Dooley, S., Dewidar, B., Hammad, S., Dediulia, T., Werle, J.,
898 Hartwig, V., Ghafoory, S., Woelfl, S., Korhonen, H. *et al.* (2020) TGF-beta2
899 silencing to target biliary-derived liver diseases. *Gut*, **69**, 1677-1690.
- 900 58. Li, X., Liu, R., Huang, Z., Gurley, E.C., Wang, X., Wang, J., He, H., Yang, H.,
901 Lai, G., Zhang, L. *et al.* (2018) Cholangiocyte-derived exosomal long
902 noncoding RNA H19 promotes cholestatic liver injury in mouse and humans.
903 *Hepatology*, **68**, 599-615.
- 904
- 905

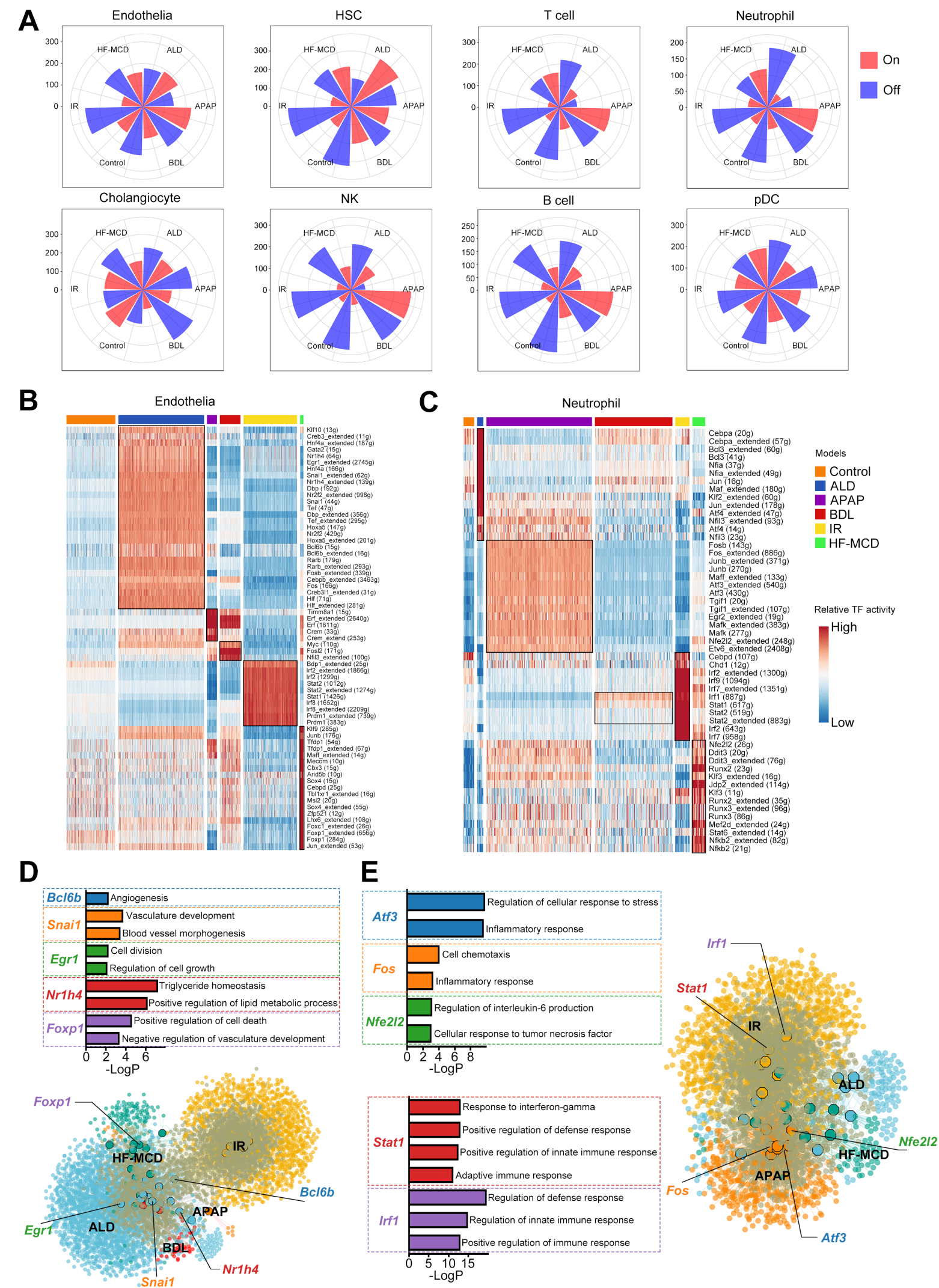
Figure 1



906 **Figure 1.** Single cell RNA-seq analysis of murine liver NPCs isolated from different
907 groups. **(A)** Illustration of the study design. **(B)** t-SNE plot visualization of 12 major
908 cell types based on 171,814 single-cell transcriptomes. MPs, mononuclear phagocytes;
909 pDC, plasmacytoid dendritic cell; HSC, hepatic stellate cell; NK, nature killer cell. **(C)**
910 Annotation by different groups. ALD, model of alcoholic liver disease; APAP, model
911 of APAP-induced acute liver injury; BDL, model of bile duct ligation-induced
912 cholestatic liver injury; IR, model of liver ischemia-reperfusion injury; MCD, model of
913 non-alcoholic steatohepatitis. **(D)** Group proportions of the 12 major cell types. **(E)**
914 Gene expression heatmap of the marker genes ($\log_{2}FC > 1.5$) for each cell type. **(F)**
915 Immunofluorescence staining of ECs markers (CD31 and LYVE1) in murine livers of
916 control, ALD and MCD groups. Nuclei were stained using DAPI (blue). Scale bars, 50
917 μm . **(G)** Immunohistochemistry of LYVE1 expression in murine livers of control, ALD
918 and MCD groups. Scale bars, 50 μm . **(H)** Immunofluorescence staining of neutrophil
919 marker S100A9 in murine livers of control, APAP and BDL groups. Nuclei were stained
920 using DAPI (blue). Scale bars, 50 μm .

921

922

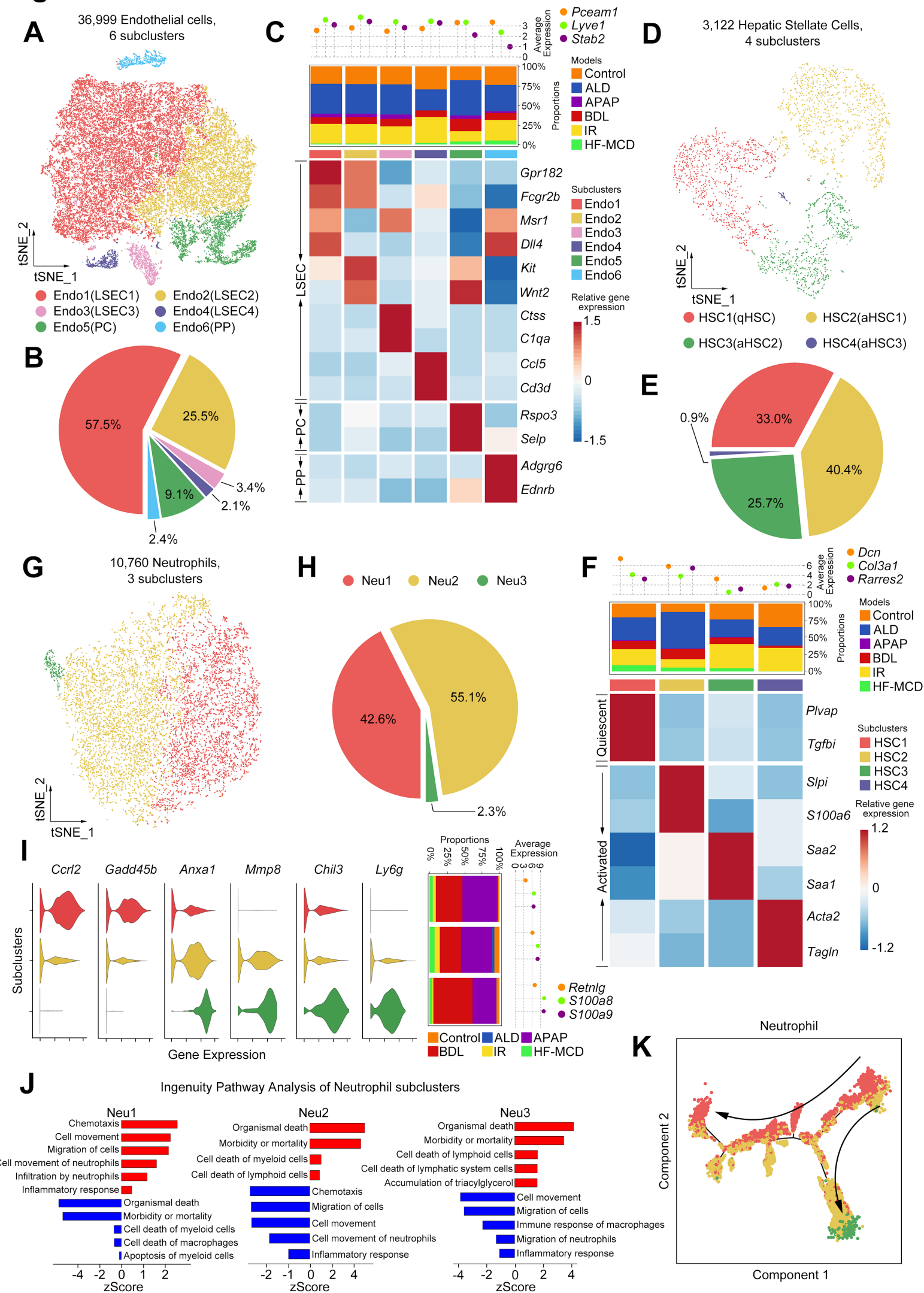


923 **Figure 2.** Changes in cellular transcription factor-target gene network in different
924 groups. **(A)** Rose diagrams visualization of the number “on/off” regulons of each cell
925 type in different groups. **(B and C)** Heatmap showing the activity of regulons of ECs
926 **(B)** and neutrophils **(C)** in different groups. Numbers between brackets indicate the
927 potential (extended) target genes for respective TFs. **(D and E)** Network visualization
928 of the inferred transcription factor-target gene networks in ECs **(D)** and neutrophils **(E)**.
929 The octagons represent TFs and the ellipses represent genes. Model-specific TFs
930 showed on **(B)** are represented by different colors. GO analysis of genes regulated by
931 model-specific TFs showing the different functional enrichment.

932

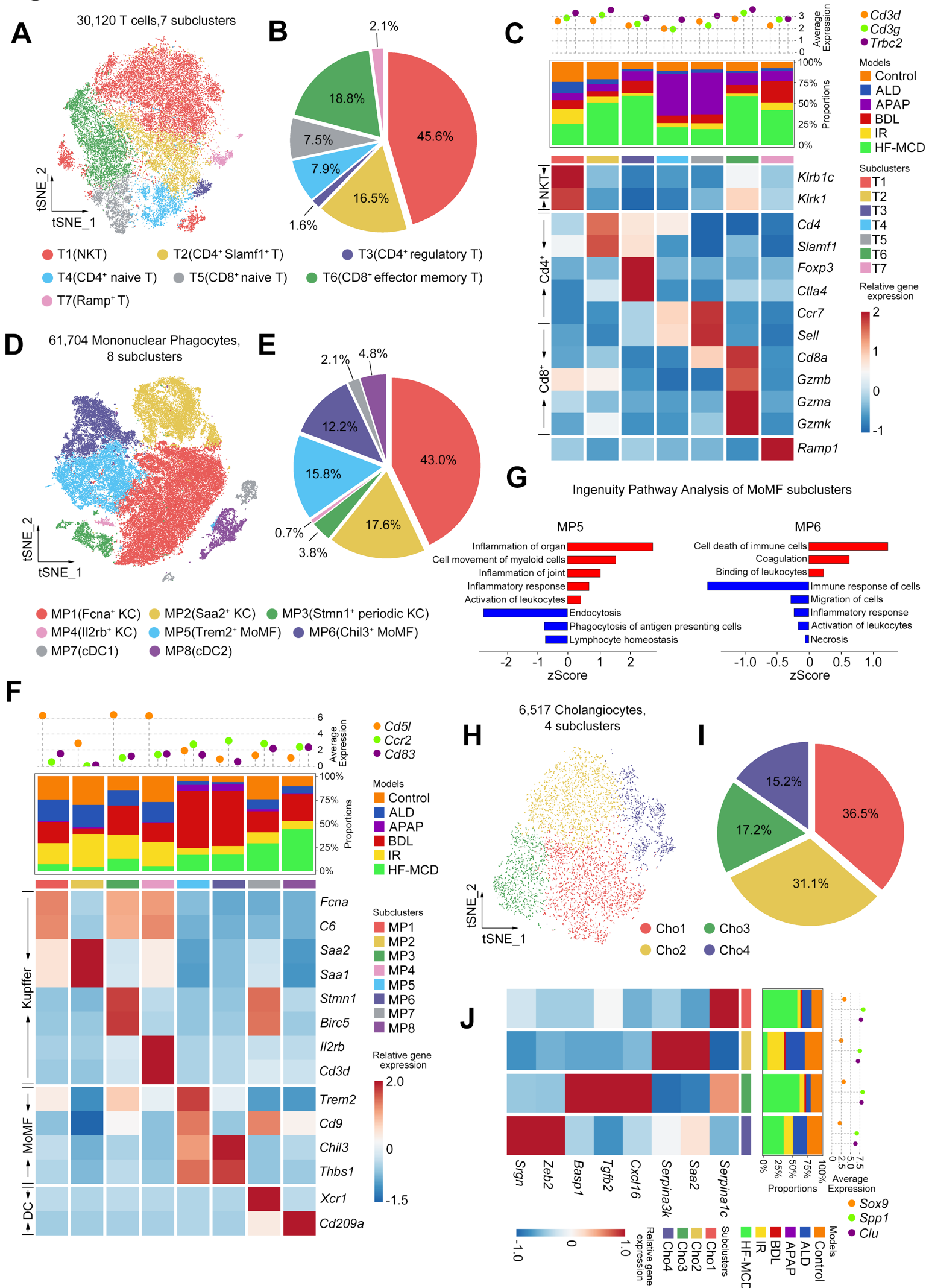
933

Figure 3



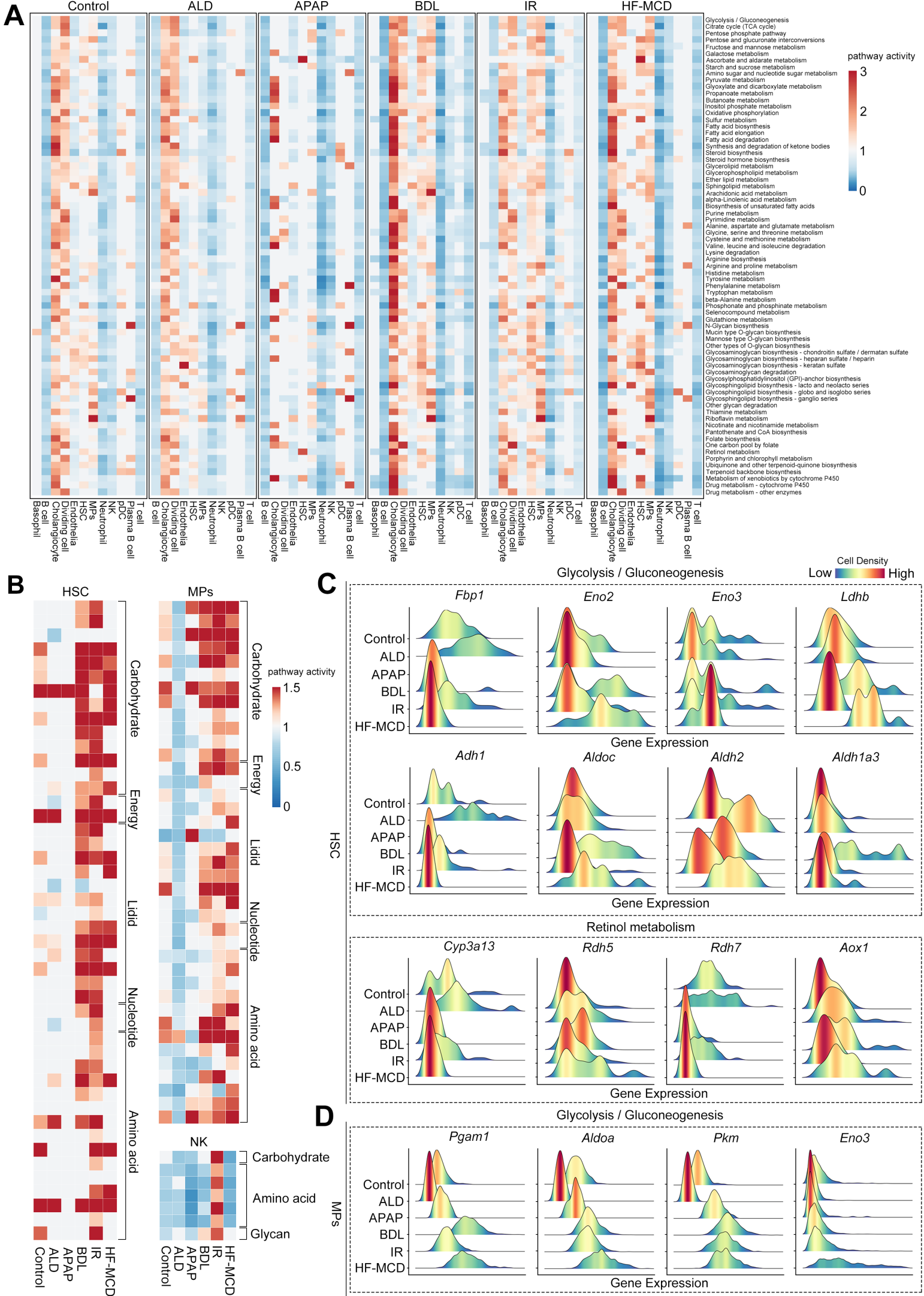
934 **Figure 3.** Subcluster analysis of endothelial cell, HSC, and neutrophil. **(A)** t-SNE plot
935 of 36,999 ECs, color-coded by cell subtypes. **(B)** Pie plot showing the proportion of
936 different ECs subtypes. **(C)** Complex heatmap of selected marker genes in each
937 endothelial cell subtype. Top: average expression of known ECs markers; Middle:
938 model proportions of each subtype; Bottom: relative expression of marker genes
939 associated with each cell subtype. LSEC, liver sinusoidal endothelial cell; PC,
940 pericentral endothelial cell; PP, periportal endothelial cell. **(D)** t-SNE plot of 3,122
941 HSCs, color-coded by cell subtypes. **(E)** Pie plot showing the proportion of different
942 HSC subtypes. **(F)** Complex heatmap of selected marker genes in each HSC subtype.
943 Top: average expression of known HSC markers; Middle: model proportions of each
944 subtype; Bottom: relative expression of marker genes associated with each cell subtype.
945 **(G)** t-SNE plot of 10,760 neutrophils, color-coded by cell subtypes. **(H)** Pie plot
946 showing the proportion of different neutrophil subtypes. **(I)** Complex violin plot of
947 selected marker genes in each neutrophil subtype. Left: expression of marker genes
948 associated with each cell subtype; Middle: model proportions of each subtype; Right:
949 average expression of known neutrophil markers. **(J)** Ingenuity Pathway Analysis of
950 each neutrophil subtype. **(K)** Pseudotime analysis of neutrophils showing the trajectory
951 from N1 to N2.
952
953

Figure 4



954 **Figure 4.** Subcluster analysis of T cell, MPs, and cholangiocyte. **(A)** t-SNE plot of
955 30,120 T cells, color-coded by cell subtypes. **(B)** Pie plot showing the proportion of
956 different T cell subtypes. **(C)** Complex heatmap of selected marker genes in each T cell
957 subtype. Top: average expression of known T cell markers; Middle: model proportions
958 of each subtype; Bottom: relative expression of marker genes associated with each cell
959 subtype. NKT, nature killer T cell; Cd4⁺, Cd4⁺ T cell; Cd8⁺, Cd8⁺ T cell. **(D)** t-SNE plot
960 of 61,704 MPs, color-coded by cell subtypes. **(E)** Pie plot showing the proportion of
961 different MPs subtypes. **(F)** Complex heatmap of selected marker genes in each MPs
962 subtype. Top: average expression of known MPs markers; Middle: model proportions
963 of each subtype; Bottom: relative expression of marker genes associated with each cell
964 subtype. Kupffer, kupffer cell; MoMF, recruited monocyte-derived macrophage; DC,
965 dendritic cell. **(G)** Ingenuity Pathway Analysis of each MoMF subtype. **(H)** t-SNE plot
966 of 6,517 cholangiocytes, color-coded by cell subtypes. **(I)** Pie plot showing the
967 proportion of different cholangiocyte subtypes. **(J)** Complex heatmap of selected
968 marker genes in each cholangiocyte subtype. Left: relative expression of marker genes
969 associated with each cell subtype; Middle: model proportions of each subtype; Right:
970 average expression of known cholangiocyte markers.
971
972

Figure 5

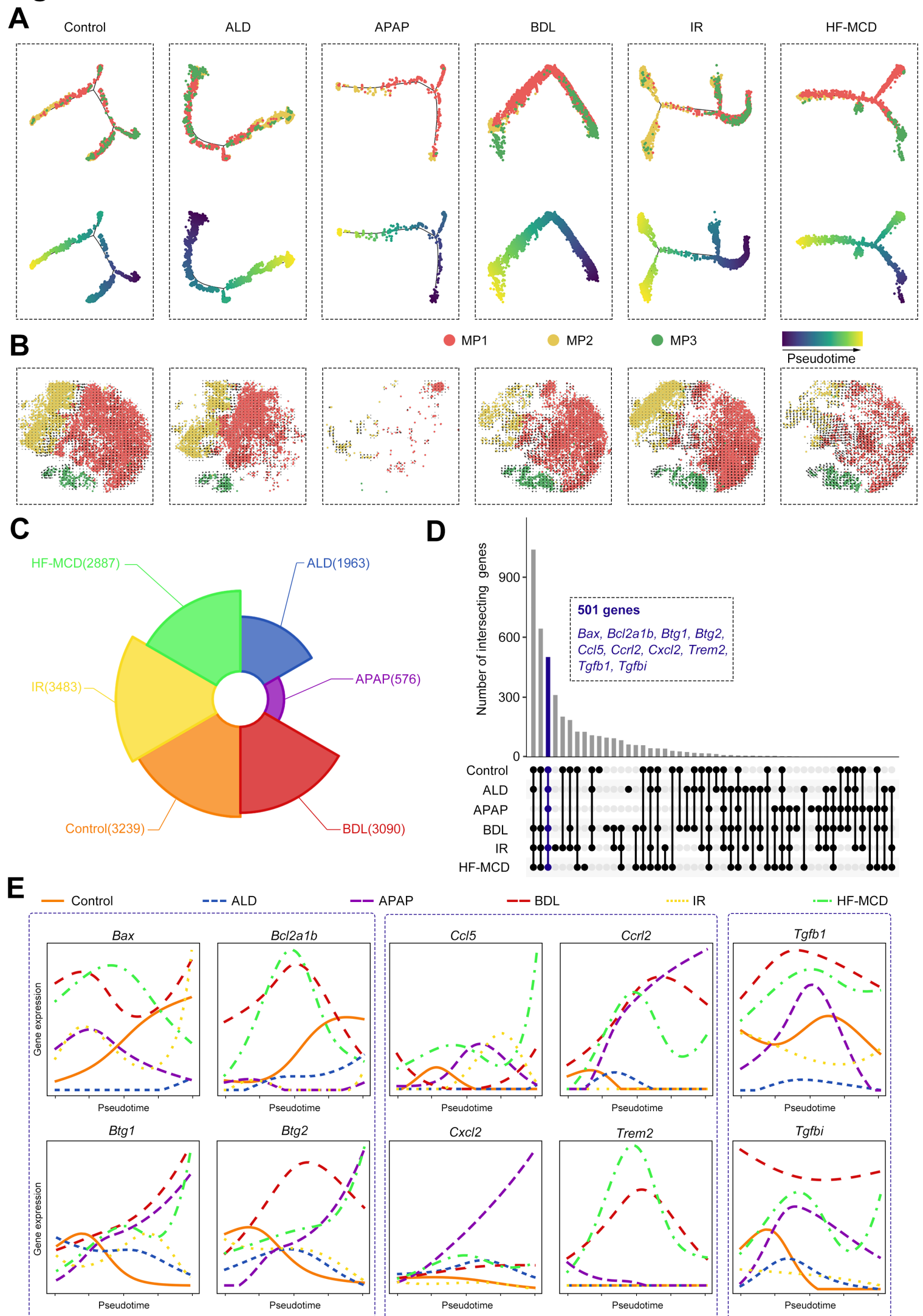


973 **Figure 5.** Disease-specific metabolic reprogramming of each cell type. **(A)** Metabolic
974 pathway activities of each cell type in different groups. For each metabolic pathway,
975 the pathway activity scores larger than 1 or smaller than 1 means significantly
976 upregulated or downregulated. **(B)** Metabolic pathway activities in HSC (left), MPs
977 (top right) and NK (bottom right) in different groups. **(C)** Mountain map visualization
978 of the expression of glycolysis/gluconeogenesis pathway related genes (top) and retinol
979 metabolism pathway related genes (bottom) in HSC in different groups. Color-coded
980 by cell density. **(D)** Mountain map visualization of the expression of
981 glycolysis/gluconeogenesis pathway related genes in MPs in different groups. Color-
982 coded by cell density.

983

984

985 **Figure 6.** The CCI network between non-immune cells and immune cells in murine
986 livers. **(A)** Heatmap showing the relative expression of immune genes in non-immune
987 cells (endothelial cell, HSC, cholangiocyte) in different groups. **(B)** The number of
988 interaction pairs between non-immune cells and other six immune cells (B cell, MPs,
989 neutrophil, NK, pDC and T cell) in different groups. **(C)** An overview of interaction
990 network between different cells (top) and the interactions between HSC and immune
991 cells (bottom). The line thickness is proportional to the number of interactions between
992 two cell types. **(D)** Dot plot displaying the specific ligand-receptor interactions between
993 HSC and immune cells in different groups. Size of the dot represents statistical
994 significance of the indicated interactions and color of the dot represents the total mean
995 of the individual partner average expression values in the corresponding interacting
996 pairs of cell types.
997
998



999 **Figure 7.** Trajectory analysis of KCs in different groups. **(A and B)** Trajectory
1000 inference of 3 KC subtypes (MP1, MP2 and MP3) using monocle **(A)** and RNA velocity
1001 **(B)**, colored by cell types or pseudotime. RNA velocity field (black arrows) were
1002 visualized on t-SNE plot of 3 KC subtypes. **(C)** The number of genes significantly
1003 differentially expressed along the pseudotime in different groups (q -value < 0.05). **(D)**
1004 Upset plot of intersections between the genes showed in **(C)** in each group. Blue bar:
1005 501 intersecting genes in 6 groups, some of which relate to apoptosis, inflammation
1006 and fibrosis were list in blue. **(E)** Expression profiles of apoptosis-related genes (left),
1007 inflammation-related genes (middle) and fibrosis-related genes (right) along the
1008 pseudotime in 6 groups.
1009